

Total pressure in thermionic orificed hollow cathodes: controlling mechanisms and their relative importance

Pierre-Yves C. R. Taunay,^{a)} Christopher J. Wordingham, and Edgar Y. Choueiri

Electric Propulsion and Plasma Dynamics Laboratory, Princeton University, Princeton, New Jersey 08544, USA.

A statistical analysis is conducted to identify which physically relevant non-dimensional parameters influence the total (neutral, ion, and electron) static pressure inside thermionic orificed hollow cathodes. It is critical to uncover and order the importance of the physical mechanisms that affect the pressure inside hollow cathodes because it influences the plasma attachment length, the electron temperature, and the sheath potential. These plasma parameters, in turn, affect the emitter lifetime. A principal component analysis of total pressure data obtained from the literature reveals that four non-dimensional variables can account for most of the variation in the total-to-magnetic pressure ratio over five orders of magnitude. The relevant variables are identified with a backward stepwise selection process and an exhaustive grid search and include, by order of importance: the gasdynamic-to-magnetic pressure ratio, the ratio of the mass flow rate to the discharge current, the orifice-to-insert diameter ratio, and the orifice Reynolds number. It is also shown, using various models and regression analyses, that empirical, Poiseuille, or isentropic flow models should not be used for predictive cathode design work. The data-driven study suggests that, while viscous effects may be important, the variation in those effects between cathodes are negligible compared to the effects of the modification of the gas constant due to the plasma, the transitional flow, the flux of heavy species on the orifice plate, and the Lorentz force.

I. INTRODUCTION

A variety of industrial and scientific applications use thermionic orificed hollow cathodes: neutral beam injectors for fusion devices,^{1–3} surface processing,^{4–6} and electric space propulsion.^{7,8} These cathodes consist of a hollow tube capped by an orifice plate and in which a low-work-function material is inserted. A “keeper” electrode is placed downstream of the cathode orifice to initiate the discharge and to prevent high-energy ions from sputtering the orifice plate. The insert material is brought to emitting temperatures with an external heater and a neutral gas is then introduced into the tube before the discharge is established with the keeper and an external anode.

In the context of electric space propulsion, the reliable operation of hollow cathode neutralizers and plasma sources is critical for successful long-term operation of Hall and ion thrusters. Missions with operational lifetimes of up to 100 kilo-hours^{9,10} without servicing and with estimated thruster power of 100–200 kW¹¹ (or, equivalently, discharge currents of up to 800 A¹²) have been proposed. While Hall thrusters are approaching this power level,^{13–15} the lifetime of high-current cathodes has been estimated to be only tens of kilo-hours. To enable next-generation missions, there is a critical need to increase cathode performance for the combined discharge current and lifetime requirements.

The lifetime of thermionic orificed hollow cathodes is limited by erosion of external surfaces, and, *fundamentally*, by the evaporation and/or sputtering of the thermionic emitter. The attachment length, or the length

over which the plasma is dense enough to “absorb” all emitted electrons, is a measure of the plasma coupling to the emitter. Under the reasonable assumptions of constant insert pressure and charge-exchange-dominated ambipolar diffusion, the attachment length (defined as the plasma density decay length scale) depends predominantly on the neutral gas pressure, P_n , and the insert geometry.¹⁶ The neutral gas pressure can be estimated in both the cathode insert and in the orifice regions from the total pressure and ionization fraction. The latter may be estimated with a 0-D model (see, *e.g.*, 12). Methods of calculating the total pressure include: an empirical relationship designed for a mercury hollow cathode,^{17–21} isentropic²² or isothermal^{23,24} flow models, Poiseuille flow theory,^{25–27} a modification of Poiseuille flow theory^{28,29} (to take into account compressibility and molecular flow effects), an “equivalent temperature” or modified specific gas constant approach taking into account the ionization fraction,^{23,24,30,31} and a hybrid framework that combines scaling laws for both electron temperature and attachment length¹⁶ with a control-volume-based model of the insert and orifice plasma.¹²

The empirical models to compute the total pressure suggested by Siegfried and Wilbur^{17–21} for mercury hollow cathodes, and by Friedly³² and Patterson and Fearn³³ for xenon cathodes, use fits based on individual cathodes. The resulting relationships from these models cannot be generalized to other cathodes or operating conditions, as we later show in Section III.

The isentropic flow model of 22 relies on the assumptions that the flow is choked at the outlet plane, that the flow rate is sufficient to ensure continuum flow in the orifice region, and that both viscous losses and heat addition due to Joule heating are negligible. Similar assumptions are made in 23 and 24 for an isothermal flow. The choked-flow assumption is justified as long as the ratio of

^{a)}Electronic mail: ptaunay@princeton.edu

upstream stagnation pressure P_0 to vacuum background pressure P_b satisfies:

$$\frac{P_0}{P_b} > G \equiv \left(\frac{\gamma + 1}{2} \right)^{\gamma/(\gamma-1)}, \quad (1)$$

where γ is the ratio of heat capacities. This condition is met for all cathodes operating in vacuum: for monatomic propellants, $\gamma = 5/3$ and $G = 2.05$. Because most cathodes operate at an internal pressure P_0 in the range of 1–100 Torr, in a vacuum chamber with $P_b \approx 10^{-5}$ Torr or lower or in the vacuum of space, $P_0/P_b \gg G$.

For most cathodes, however, the continuum assumption in the orifice is not guaranteed to hold: the Knudsen number, Kn , is in the range of 0.01–10, as shown in Figure 2(a), which indicates that the flow is in the transition regime from continuum to molecular flow. The values shown in Figure 2(a) are computed using a set of experimental data from Siegfried and Wilbur's cathode operating on mercury³⁴ and argon and xenon,²¹ Friedly's cathode,³² Salhi's cathode operating on xenon and argon,²⁴ Domonkos's SC012, EK6, and AR3 cathodes,²⁸ the T6 cathode from the Royal Aerospace Establishment,^{33,35} the NSTAR and NEXIS cathodes from the Jet Propulsion Laboratory (JPL),^{36–40} and the JPL 1.5 cm cathode.^{41,42} The neutral gas temperature is estimated to be either three times the maximum insert wall temperature (in Kelvin),²⁵ or 3000 K if wall temperature data are unavailable. We use the following expression to estimate Kn :⁴³

$$Kn = \frac{Ma}{Re} = \frac{16}{5} \sqrt{\frac{\gamma}{2\pi}}, \quad (2)$$

where Re and Ma are the Reynolds and Mach numbers, respectively. We assume that the flow is sonic in the orifice ($Ma = 1$). The dynamic viscosity for the Reynolds number is calculated using results from Stiel and Thodos⁴⁴ for xenon and argon. For mercury vapor, we use the Chapman-Enskog method applied to the Lennard-Jones 12-6 potential (for simplicity) with $\sigma = 2.898 \text{ \AA}$ and $\epsilon/k_B = 851.0 \text{ K}$.⁴⁵ This method produces good agreement with experimental viscosity data for temperatures less than 1,500 K as shown in Figure 1. We are not aware of the existence of data for temperatures higher than 1,500 K for mercury.

It has been suggested that viscosity is an important contributor to the flow dynamics inside the cathode in 2-D simulations in 39. Computed Reynolds numbers, Re , in Figure 2(b) indicate that the flow through the cathode can be considered laminar ($Re \ll 1000$) and that viscous effects may be important ($0.1 < Re < 10$). The assumptions required for Poiseuille flow analysis appear to be valid in the section upstream of the plasma in the cathode tube: the flow is incompressible, fully-developed, laminar, and with a no-slip condition at the wall. Poiseuille flow theory, however, is not applicable in the orifice or insert plasma regions: in the orifice region, the flow may be laminar and may feature a no-slip

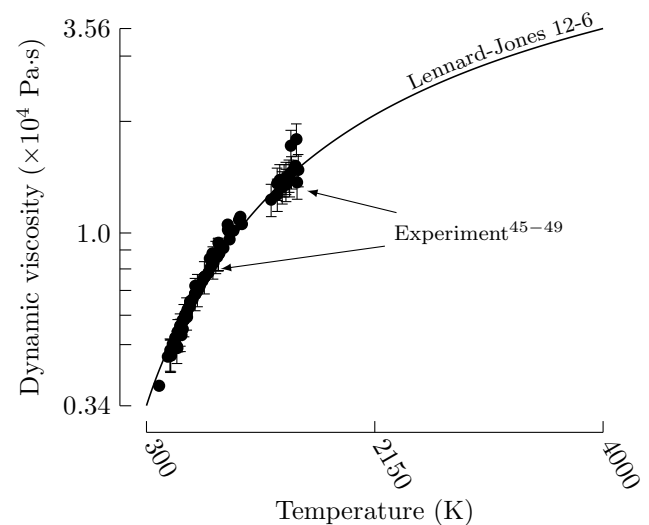


FIG. 1: Viscosity of mercury vapor computed using the Chapman-Enskog method applied to a Lennard-Jones 12-6 potential. Experimental data from 45–49. Adapted from “Pierre-Yves C. R. Taunay, *Scaling Laws in Orificed Thermionic Hollow Cathodes*, Ph.D. dissertation, Princeton University, 2020.”⁵⁰ Copyright 2020, Pierre-Yves C. R. Taunay.

condition at the wall but it becomes compressible and is not fully-developed. Poiseuille flow theory also assumes adiabatic flow, which is not valid in most regions of the cathode. The flow transitions from a low Mach number in the insert region to a sonic condition at the orifice outlet and therefore shows strong compressibility effects. The length over which the flow travels before becoming fully-developed, or “entrance length”, can be estimated with:⁵¹

$$L_{fd} \approx 0.06 Re d_o \quad (3)$$

The range of ratio of L_{fd} to the orifice length L_o is shown in Figure 2(c) for various cathodes. For most cathodes the effect of the orifice constriction invalidates the assumption of fully-developed flow over the entire length of the orifice. The Poiseuille flow model also does not take into account plasma effects, and therefore fails to capture the dependence of the total pressure on gas/plasma properties and discharge current.

More complex theoretical models such as those proposed by Domonkos^{28,29} and Albertoni *et al.*,^{30,31} and in our own work¹² attempt to address some of the aforementioned issues. Domonkos suggests combining Poiseuille flow with a choked flow condition at the orifice outlet, and adds a modification to the obtained result to account for the insert-to-orifice constriction and transition to molecular flow.

Albertoni *et al.*³¹ introduce the effect of the plasma through the ionization fraction and electron temperature, which are computed as part of a 0-D model. The relationship proposed by Albertoni *et al.* is used to compute

This is the author's peer reviewed, accepted manuscript. However, the online version of record will be different from this version once it has been copyedited and typeset.

PLEASE CITE THIS ARTICLE AS DOI: 10.1063/5.0067271

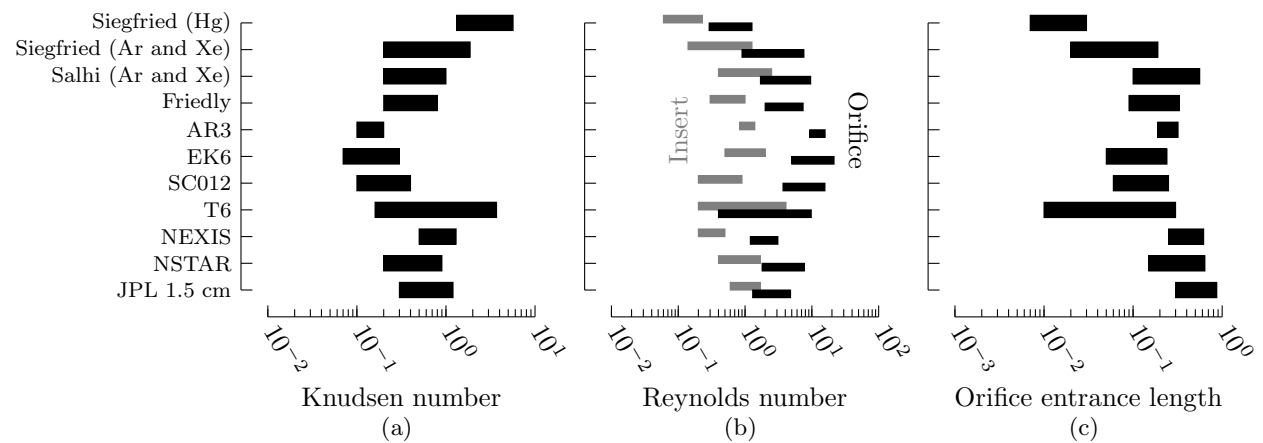


FIG. 2: Range of (a) orifice Knudsen number, (b) Reynolds number for both insert and orifice, and (c) orifice entrance length (as a fraction of total orifice length). Adapted from “Pierre-Yves C. R. Taunay, *Scaling Laws in Orificed Thermionic Hollow Cathodes*, Ph.D. dissertation, Princeton University, 2020.”⁵⁰ Copyright 2020, Pierre-Yves C. R. Taunay.

the total static pressure and is valid at the orifice outlet where choked flow conditions are assumed. This model relies on Domonkos’s modified Poiseuille flow model to predict the pressure drop across the orifice, and therefore suffers from the problems associated with violating the required assumptions in the orifice section. Use of the Poiseuille flow model with choked flow as a downstream boundary condition may also be fundamentally inconsistent if the upstream stagnation pressure is used in the choked flow calculation.

An analytical description of the flow within hollow cathodes is challenging: heat addition from Joule heating in the orifice, frozen flow and wall losses due to ionization and plasma sheath fluxes, a transition from incompressible to sonic flow over the length of a short orifice, viscous effects, and a transition to molecular flow all complicate the governing flow equations. We have presented a self-consistent theoretical framework in 12 that attempts to include some of these effects to study scaling laws for the total pressure within cathodes. The pressure is modeled based on the combined three-fluid flow and is shown to be a combination of magnetic pressure, gasdynamic pressure modified to take into account transitional flow and plasma effects, and a term that corresponds to the momentum flux of heavy species on the orifice plate. The present study is a complementary approach to the aforementioned theoretical framework. Using a data-driven perspective, our goal is to confirm the relative importance of the parameters that appear in the theoretical derivation presented in 12.

In this work, we use a data-driven approach to identify the physical mechanisms that influence the total static pressure inside orificed hollow cathodes. We gather experimental data and uncover non-dimensional parameters in Section II. We demonstrate in Section III that previous empirical and theoretical models cannot account for the variation in the total pressure data. We then

perform a statistical analysis to extract the most pertinent non-dimensional variables, rank their relevance, and infer the relative importance of the controlling mechanisms. We finally discuss the physical meaning of the non-dimensional variables in Section IV and show that a theoretical framework that accounts for the modification of the gas constant due to the plasma, the transitional flow, the flux of heavy species on the orifice plate, and the Lorentz force can account for the variation in the total pressure data.

II. PRESSURE DIMENSIONAL ANALYSIS

A. Experimental dataset

We have compiled a database of existing data from the available literature containing 422 data points and spanning 40 years of hollow cathode experimental work for multiple gases (mercury, argon, xenon). The total pressures, discharge currents, and mass flow rates are in the range of 0.7–610 Torr, 0.5–307 A, 0.05–6.5 mg/s (0.35–218 sccm), respectively. In addition to the existing data, we have collected data from our own hollow cathode (Princeton Large Hollow Cathode, PLHC)¹² operating at up to 307 A of discharge current on argon. We have described in details the database in 52, and we give a permanent DOI that links to the database in the “Data Availability” section of the manuscript.

We define the pressure as the total static pressure upstream of the cathode emitter. That pressure is typically measured upstream of the cathode active zone, sometimes multiple cathode lengths away from the plasma (see, *e.g.*, 28). In most cases, however, feed-system losses are small. For the cathodes described in 28, the feed-system loss is estimated to be less than 0.01% of the measured pressure (28, p.26). For the NSTAR, NEXIS,

JPL 1.5 cm, PLHC, Salhi's cathodes, the pressure measurement point is situated less than 20 cm away from the cathode active zone. Assuming an upper bound for the gas temperature (upstream of the active zone) of 1,000 K and a Poiseuille flow model (which is valid upstream of the active zone), the feed-system loss is estimated to be, on average, 3%. We therefore assume that the pressure data are representative of the total static pressure upstream of the active zone.

B. Π products

As observed in the experimental data, we expect the cathode pressure to exhibit dependence on geometry, mass flow rate, discharge current, gas species, gas temperature, and viscosity. We neglect the effect of an externally applied magnetic field on the total pressure: Friedly³² did not observe any effect of the magnetic field on the total pressure, and the Hall parameter in the insert and orifice regions for both electrons and ions is small.^{53–55} We therefore consider a general expression for the pressure in the insert region,

$$P = f(d_o, d_c, L_o, \dot{m}, I_d, M, a, \epsilon_{iz}, \mu, \mu_0), \quad (4)$$

where d_o and d_c are the orifice and insert diameters, respectively, L_o is the orifice length, I_d is the discharge current, \dot{m} is the mass flow rate, M is the atomic mass of the propellant considered, a is its speed of sound, ϵ_{iz} is its (first ground-state electron-impact) ionization energy in V, μ is the dynamic viscosity, and μ_0 is the permeability of vacuum. All quantities are in S.I. units unless otherwise specified.

There are four physical dimensions (mass, length, time, charge) and 11 parameters. The Buckingham Π theorem⁵⁶ indicates that there should be seven non-dimensional Π -products. We use Ipsen's method⁵⁷ to find the Π -products by successively eliminating physical dimensions from Equation 4. We consider the following Π -products:

$$\Pi_1 = \frac{P}{P_{mag}}, \quad (5)$$

$$\Pi_2 = \frac{d_o}{d_c}, \quad (6)$$

$$\Pi_3 = \frac{d_o}{L_o}, \quad (7)$$

$$\Pi_4 = \left(\frac{\dot{m}e}{MI_d} \right)^2 \left(\frac{Md_o}{\mu_0 e^2} \right), \quad (8)$$

$$\Pi_5 = \frac{P_{gd}}{P_{mag}}, \quad (9)$$

$$\Pi_6 = \left(\frac{P_{ionization}}{P_{mag}} \right) \left(\frac{L_o}{d_o} \right), \text{ and} \quad (10)$$

$$\Pi_7 = \text{Re}, \quad (11)$$

where we defined the magnetic and gasdynamic pressures, and orifice Reynolds number as:

$$P_{mag} = \frac{\mu_0 I_d^2}{\pi^2 d_o^2}, \quad (12)$$

$$P_{gd} = \frac{4\dot{m}a}{\pi d_o^2}, \text{ and} \quad (13)$$

$$\text{Re} = \frac{4\dot{m}d_o}{\mu\pi d_o^2}, \quad (14)$$

respectively. We defined an “ionization pressure” as:

$$P_{ionization} = \frac{4e\epsilon_{iz}}{\pi d_o^2 L_o}. \quad (15)$$

We recognize the ratio of total to magnetic pressures in the orifice as the first Π -product. The second and third Π -products are geometric aspect ratios. The term $(\dot{m}e/MI_d)$ in the fourth Π -product is the total heavy-particle number flux divided by that of electrons. It is related to the ionization fraction and mass utilization efficiency. The second term in Π_4 involves both geometry and gas species. The fifth Π -product is the ratio of gasdynamic to magnetic pressures. The numerator of Π_6 is the ionization energy density inside the orifice. It is multiplied by the inverse of Π_3 . The seventh Π -product is the orifice Reynolds number and accounts for viscous effects.

The above process could be repeated using a different order for removing the physical dimensions. This would result in a different set of Π -products. However, we have found that the Π -products we obtained are the most physically meaningful.

C. Neutral gas temperature

The neutral gas temperature is necessary to calculate the speed of sound that appears in P_{gd} . It is estimated to be three times that of the insert wall temperature (in Kelvin), T_c , as suggested in 25 (p.465). For each cathode, we first seek an estimate of the wall temperature based on the available data. For the NSTAR and NEXIS cathodes, experimental and numerical fits for the wall temperature in Kelvin are given in 58 and 25 (p.301) as:

$$T_{\text{NSTAR}} [\text{K}] = 1191.6 I_d^{0.0988}, \text{ and} \quad (16)$$

$$T_{\text{NEXIS}} [\text{K}] = 1370 + 3.971 \times 10^{-7} I_d^6, \quad (17)$$

respectively. These fits are used when no experimental data are directly available. Orifice plate temperature is reported in 42 as a function of both mass flow rate and discharge current for the JPL 1.5 cm cathode. A linear fit captures the variation of the data:

$$T_{\text{JPL 1.5 cm}} [^\circ\text{C}] = 1144 + 5.56 I_d. \quad (18)$$

We use this fit for the wall temperature for the cases reported in 41 because the cathodes are identical. Because

the geometry of the AR3, EK6, and SC012 cathodes from 28 are similar, we simply use the average value of the available temperature data when no data are available. A similar procedure is performed for Salhi's cathode²⁴ and Siegfried's cathode operating with noble gases,²¹ separating the cases with different orifice sizes and different operating species:

$$T_{\text{AR3, EK6, SC012}} = 980^\circ\text{C}, \quad (19)$$

$$T_{\text{Salhi (Ar), } d_o=0.76\text{mm}} = 891^\circ\text{C}, \quad (20)$$

$$T_{\text{Salhi (Ar), } d_o=1.21\text{mm}} = 999^\circ\text{C}, \quad (21)$$

$$T_{\text{Salhi (Xe)}} = 991^\circ\text{C}, \text{ and} \quad (22)$$

$$T_{\text{Siegfried (Xe)}} = 1097^\circ\text{C}. \quad (23)$$

If no temperature data are available (as is the case for the T6 and our cathode), the temperature is estimated to be that which yields the total discharge current from thermionic emission:

$$I_d = D_{RD} T_c^2 \exp\left(\frac{-e\phi_w}{k_B T_c}\right) 2\pi r_c L_{\text{eff}}, \quad (24)$$

where r_c is the insert radius, L_{eff} is the attachment length, ϕ_w is the work function, D_{RD} is the Richardson-Dushman constant, T_c is the wall temperature, and k_B is the Boltzmann constant. The attachment (or emission) length may be estimated to 0th order as the insert radius:^{16,59} $L_{\text{eff}} \approx r_c$.

III. PRESSURE STATISTICAL ANALYSIS

A. Review of previous models

We start our analysis by reviewing previous empirical and theoretical models and demonstrating that they cannot capture the behavior of the nondimensionalized total pressure with operating conditions for the entire dataset.

1. Empirical models

We consider the total pressure models from Siegfried and Wilbur,^{17–21} Capacci *et al.*,⁶⁰ and Patterson and Fearn³³. The total pressure for those models is given by

$$P_S = \frac{\dot{m}_A}{d_o^2} (\beta_0 + \beta_1 I_d), \quad (25)$$

$$P_C = \frac{\dot{m}_A}{d_o^2} (\beta_0 + \beta_1 I_d + \beta_2 I_d^2), \text{ and} \quad (26)$$

$$P_P = \beta_0 + \beta_1 \dot{m} + \beta_2 \dot{m}^2 + \beta_3 \dot{m} I_d + \beta_4 I_d + \beta_5 I_d^2, \quad (27)$$

respectively. The constants β_k are to be determined with a non-linear fit of the non-dimensional data. The mass flow rate \dot{m}_A is given in units of equivalent-amperes.

We normalize the pressure models by the magnetic pressure:

$$\Pi_{1S} = \frac{\dot{m}_A}{P_{\text{mag}} d_o^2} (\beta_0 + \beta_1 I_d), \quad (28)$$

$$\Pi_{1C} = \frac{\dot{m}_A}{P_{\text{mag}} d_o^2} (\beta_0 + \beta_1 I_d + \beta_2 I_d^2), \text{ and} \quad (29)$$

$$\Pi_{1P} = \frac{1}{P_{\text{mag}}} (\beta_0 + \beta_1 \dot{m} + \beta_2 \dot{m}^2 + \beta_3 \dot{m} I_d + \beta_4 I_d + \beta_5 I_d^2), \quad (30)$$

and perform a non-linear fit in logarithmic space (*i.e.*, we fit $\log_{10}(\Pi_1)$) with the `lmfit` Python package⁶¹ and the dataset described in the previous section. The R-squared value (R^2) and average total pressure error of each model are reported in Table I. Both values are calculated with the dimensionless and dimensional expressions, respectively. The models from both Siegfried and Wilbur and Capacci *et al.* converge to the same values for β_0 and β_1 , with $\beta_2 \approx 0$ for the latter model. They therefore have an identical R^2 and average error. The dimensionless expressions are illustrated in Figure 4, where the straight dashed line indicates perfect agreement between experimental data and model.

None of the proposed models are able to account for the variation in the data. They all display either a high R^2 and average error, which indicates that the model is lacking a feature necessary to account for data variation, or have a high average error and low R^2 value, indicating poor agreement overall. These models, however, perform better on a per-cathode basis. For example, the empirical models feature an R^2 of 0.63–0.95 and an average error of 14.1–41.8% when applied to the T6 cathode alone.

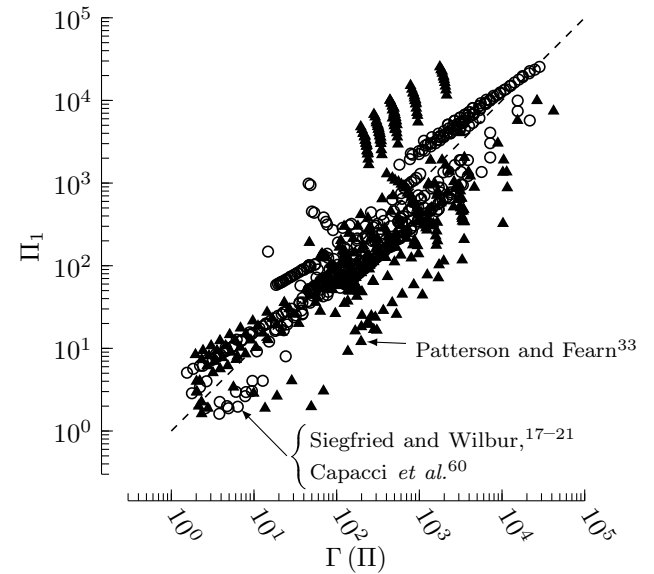


FIG. 3: Comparison between Π_1 and its estimate as obtained with previous empirical models.

TABLE I: R^2 and average error for the studied flow models.

Approach	Flow model	R^2	Average error (%)
Empirical	Siegfried and Wilbur ¹⁷⁻²¹	0.89	69.0
	Capacci <i>et al.</i> ⁶⁰	0.89	69.0
	Patterson and Fearn ³³	0.48	231.3
	Power law (this work)	0.97	22.7
Theoretical	Isentropic	0.36	65.1
	Poiseuille	0.57	57.4
	Taunay <i>et al.</i> ¹²	0.98	25.4

2. Poiseuille and isentropic flow

We now consider two commonly used theoretical models for the total pressure, Poiseuille flow and isentropic flow, as both can be expressed directly in terms of the derived Π -products. We emphasize that the Poiseuille flow model cannot, in practice, be applied in the orifice for the reasons discussed in the Introduction. It is instructive, however, to find an expression for the ratio of total-to-magnetic pressure that depends only on the Π -products. The pressure expressions as derived from the isentropic and Poiseuille models are given by:

$$P = C_{if} \frac{\dot{m}a}{\pi r_o^2}, \text{ and} \quad (31)$$

$$P = C_P \left(\frac{L_o}{r_o} \right)^{1/2} \frac{1}{\text{Re}^{1/2}} \frac{\dot{m}a}{\pi r_o^2}, \quad (32)$$

respectively. The constants C_{if} and C_P are the scaling constants:

$$C_{if} = \frac{1}{\gamma} \left(\frac{\gamma + 1}{2} \right)^{\gamma/(\gamma-1)} \approx 1.23, \quad (33)$$

$$C_P = 4\sqrt{2}\gamma^{-1/2} \approx 3.1. \quad (34)$$

To obtain Equation 31 the static temperature is used in the definition of the speed of sound. We assume that the static temperature (and, therefore, speed of sound) is constant in the orifice and use the orifice diameter as the characteristic length for the orifice Reynolds number to obtain Equation 32. The results from the isentropic and Poiseuille flow models depend only on Π_5 , and on Π_3 , Π_5 , and Π_7 , respectively:

$$\Pi_1 = C_{if} \Pi_5, \quad (35)$$

$$\Pi_1 = C_P \Pi_3^{-1/2} \Pi_5 \Pi_7^{-1/2}. \quad (36)$$

Neither model includes a direct dependence on the plasma quantities (except possibly through the gas temperature and/or sound speed) and therefore neither result depends on discharge current. The R^2 and average total pressure error of each model are reported in Table I. The low values of R^2 and high average error for both isentropic and Poiseuille flow indicate that they do not

adequately capture the variation of the total pressure inside hollow cathodes. The dimensionless expressions are illustrated in Figure 4, where the straight dashed line indicates perfect agreement between experimental data and model.

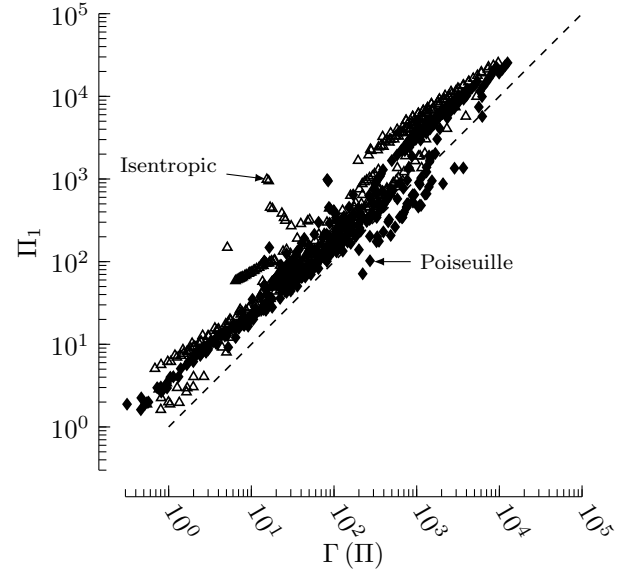


FIG. 4: Comparison between Π_1 and its estimate as obtained with an isentropic ($\Gamma(\Pi) = C_{if}\Pi_5$) and a Poiseuille flow model ($\Gamma(\Pi) = C_P\Pi_3^{-1/2}\Pi_5\Pi_7^{-1/2}$).

B. Power law approach

Because both Equations 35 and 36 take the form of a power law, we now assume a more general form for Π_1 as a function of all Π -products:

$$\Pi_1 = C \prod_{k=2}^7 \Pi_k^{\beta_{k-1}} = \Gamma(\Pi), \quad (37)$$

where C is a scaling constant, and the β_{k-1} are exponents to be determined. After applying the base-10 logarithm to both sides of Equation 37, we obtain a linear relationship:

$$Y = \beta_0 + \sum_{k=2}^7 \beta_{k-1} X_k, \quad (38)$$

where $Y = \log_{10} \Pi_1$, $X_k = \log_{10} \Pi_k$, and $\beta_0 = \log_{10} C$. Equation 38 is a multivariate linear expression, which we fit to the experimental data using a least-squares approach. We show in Table II the least-squares coefficients along with their 95% confidence intervals as computed from the covariance matrix. The corresponding constant for the power law is $C = 1.16 \times 10^7$, and the power law may be written as:

$$\Pi_1 \approx 1.2 \times 10^7 \Pi_2^{0.79} \Pi_3^{0.23} \Pi_4^{-0.27} \Pi_5^{0.82} \Pi_6^{0.25} \Pi_7^{0.41}. \quad (39)$$

This is the author's peer reviewed, accepted manuscript. However, the online version of record will be different from this version once it has been copyedited and typeset.

PLEASE CITE THIS ARTICLE AS DOI: 10.1063/5.0067271

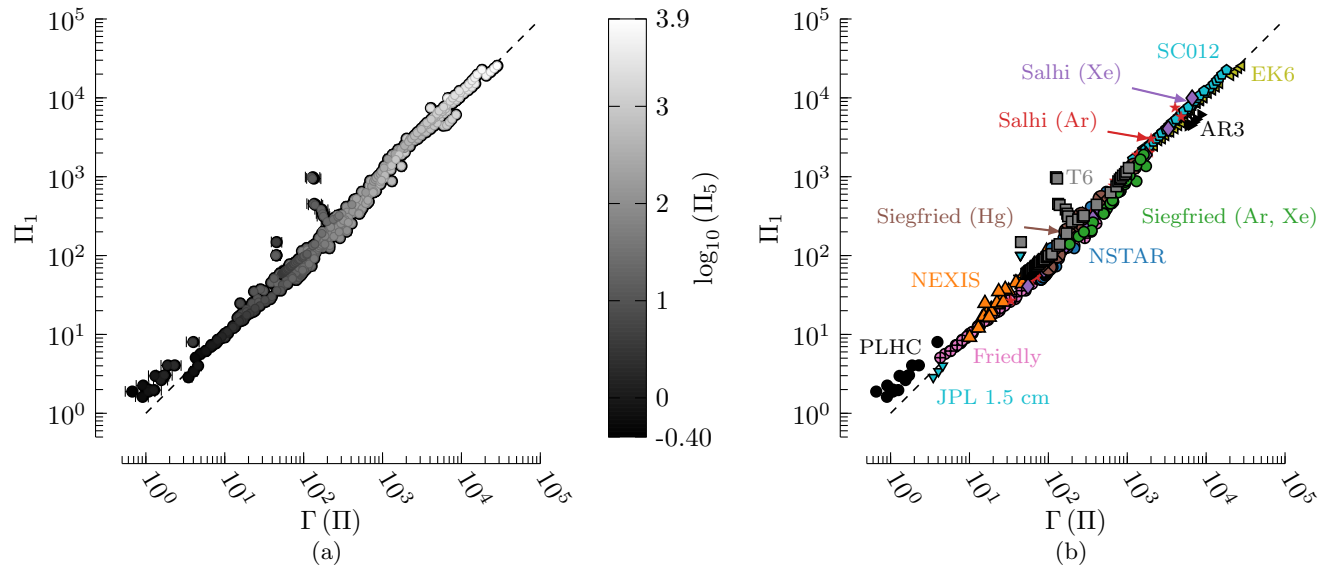


FIG. 5: Proposed power law (Equation 37) applied to the entire data set:
 $\Gamma(\Pi) = 1.2 \times 10^7 \Pi_2^{0.79} \Pi_3^{0.23} \Pi_4^{-0.27} \Pi_5^{0.82} \Pi_6^{0.25} \Pi_7^{0.41}$. Regression colored by (a) ratio of gasdynamic to magnetic pressure (Π_5), and (b) individual cathode. The horizontal error bars in (a) represent the 95% confidence interval for the predicted Π_1 value as obtained from the bootstrap method applied to the multivariate linear regression. Figures 5(a) and (b) were adapted and reproduced (respectively) from “Pierre-Yves C. R. Taunay, *Scaling Laws in Orificed Thermionic Hollow Cathodes*, Ph.D. dissertation, Princeton University, 2020.”⁵⁰ Copyright 2020, Pierre-Yves C. R. Taunay.

TABLE II: Power law coefficients and associated 95% confidence interval.

Π -product	Coefficient	Lower bound	Value	Upper bound
—	β_0	6.41	7.06	7.73
Π_2	β_1	0.70	0.79	0.88
Π_3	β_2	0.13	0.23	0.33
Π_4	β_3	-0.44	-0.27	-0.09
Π_5	β_4	0.44	0.82	1.19
Π_6	β_5	0.06	0.25	0.45
Π_7	β_6	0.34	0.41	0.47

1. Qualitative analysis

The power law fit applied to the entire experimental dataset is shown in Figures 5(a) and (b). The data collapse onto a single line, indicating good agreement with the proposed empirical relationship over a range of five orders of magnitude of Π_1 . The error bars shown in Figure 5(a) indicate the 95% confidence intervals of the predicted values as obtained with the bootstrap method. The bootstrap method consists of performing the following steps repeatedly: (i) generate a dataset of 422 randomly sampled points (with replacement) from the original dataset, (ii) perform the least-squares regression to obtain the β_k coefficients, and (iii) calculate $\hat{\Pi}_1 = \Gamma(\Pi)$, where $\hat{\Pi}_1$ is the predicted value of Π_1 . We perform those steps 50,000 times to gather statistically significant vari-

ation for $\hat{\Pi}_1$.

The groupings of data by value of Π_5 in Figure 5(a) and by cathode in Figure 5(b) show that the relationship between Π_1 and Π_5 is nearly linear. This implies that the total pressure is nearly proportional to the gasdynamic pressure. The cathodes that operate at high current (> 20 A: PLHC, Friedly's cathode, NEXIS) feature a larger magnetic pressure contribution to the total pressure than those that operate at low current (< 5 A: AR3, EK6, SC012). Because the NSTAR, T6, Salhi's, and Siegfried's cathodes all have similar dimensions, there is an accumulation of data points at the center of the plot ($\approx 50 < \Pi_1 < 1,000$).

2. Error analysis

The obtained R^2 and average error for the least-squares fit are reported in Table I. They are equal to 0.97 and 22.7%, respectively. Figure 6 shows the distribution of the absolute value of the relative pressure error both as a histogram and as a continuous distribution estimated with the Kernel Density Estimate method. It indicates that the proposed fit is mostly within a factor of 1.3 of the experimental data.

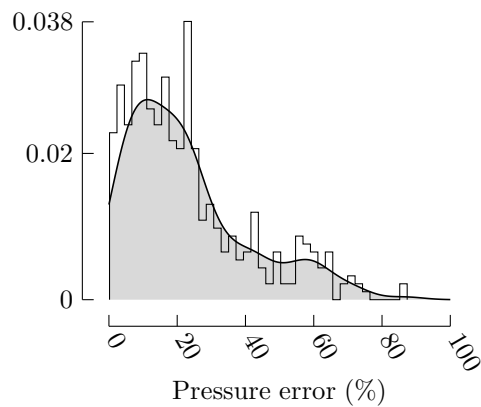


FIG. 6: Error histogram for the power-law fit (Equation 37). Reproduced from “Pierre-Yves C. R. Taunay, *Scaling Laws in Orificed Thermionic Hollow Cathodes*, Ph.D. dissertation, Princeton University, 2020.”⁵⁰ Copyright 2020, Pierre-Yves C. R. Taunay.

C. Statistical analysis

1. Principal Component Analysis

Principal Component Analysis (PCA) is a tool for dimensionality reduction. The goal of PCA is to identify the number of relevant features from a given dataset, as a smaller number of uncorrelated features can often account for most of the variation within the dataset. Figure 7 shows the explained variance as a function of the total number of principal component variables considered. PCA calculations were performed using the `scikit-learn` API⁶². With a single variable, the dataset has an explained variance of 0.825, which indicates that one parameter is enough to account for most of the variation in the data. The explained variance ceases to increase for three or more dimensions which indicates that three parameters could account for the variation in the total pressure Π -product, Π_1 . The PCA parameters are not identical to the original set of Π -products, but this suggests that we may be able to reduce the dimensionality of the original set of Π -products, as they may be correlated to one another.

2. Backward stepwise selection with randomized Π -products

The randomized selection test consists of rearranging the samples of one Π -product at a time at random, performing a linear regression (Equation 38), and calculating both the R^2 and average error. The randomization of a superfluous Π -product has little to no effect on these metrics. The process is repeated 1,000 times to generate representative values of R^2 and average error. The corresponding R^2 and average error resulting from this operation are shown in Table III. We observe that the

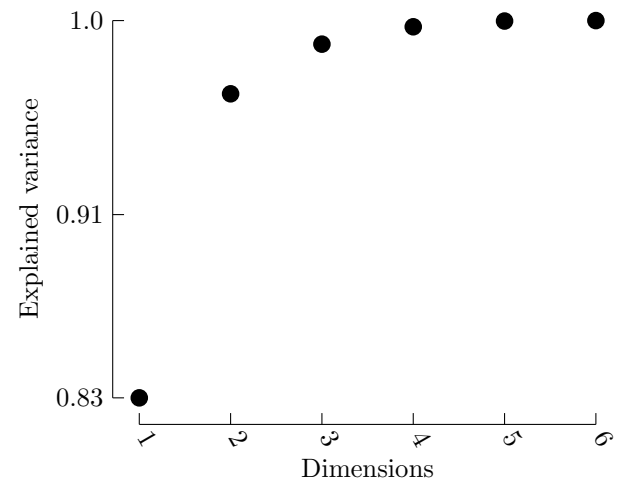


FIG. 7: Explained variance for the dataset. Reproduced from “Pierre-Yves C. R. Taunay, *Scaling Laws in Orificed Thermionic Hollow Cathodes*, Ph.D. dissertation, Princeton University, 2020.”⁵⁰ Copyright 2020, Pierre-Yves C. R. Taunay.

randomizations of Π_3 and Π_6 have the smallest effect on the overall fit.

The process can be repeated once these products are discarded. We find that both Π_2 and Π_7 have the next smallest effect on the fit during the second iteration and can also be removed from the fit without introducing large errors. The products that remain are Π_4 and Π_5 ; the latter was shown to be qualitatively important in Figure 5(a).

3. Exhaustive grid search

Methodology The results of the backward stepwise selection can be verified with an exhaustive grid search. We now apply the linear least-squares fit and consider all possible variable combinations: each Π -product may or may not be included in the power-law least-squares fit. For the six Π -products considered (Π_2 through Π_7), this corresponds to $2^6 = 64$ combinations. In practice, we exclude the case where no Π -products are included in the least-squares fit and consider a maximum of 63 possible combinations.

We use the Akaike information criterion⁶³ (AIC) to score each regression. The AIC ensures that higher complexity models are appropriately penalized when models are compared. For a linear regression, the AIC can be written as:

$$\text{AIC} = 2p + N \log(\text{MSE}), \quad (40)$$

where p is the total number of parameters in the regression (here, 2 to 7), N is the total number of samples used

TABLE III: R^2 and average error for the linear fit with a randomized Π -product. The calculated values for the unperturbed fit in each iteration are shown on the “Reference” line.

Perturbed Π -product	Iteration 1		Iteration 2	
	R^2	Average error (%)	R^2	Average error (%)
Reference	0.98	22.7	0.978	23.5
2	0.965	30.0	0.965	29.8
3	0.978	23.6	–	–
4	0.978	24.0	0.936	45.3
5	0.978	24.5	0.482	709.
6	0.979	22.4	–	–
7	0.971	29.9	0.971	30.4

for scoring, and MSE is the mean squared error:

$$\text{MSE} = \frac{1}{N} \sum_{i=1}^N (Y_i - \hat{Y}_i)^2, \quad (41)$$

where \hat{Y}_i is the predicted Y_i as calculated from Equation 38 using the input Π -products and the coefficients determined by each individual linear regression.

To reduce bias, we perform the grid search with a k -fold approach where only a fraction of the entire dataset is used at a time for a given number of variables considered. For each set of variables considered among the 63 possible combinations, the linear regression is performed on a subset of the data (training phase) and is scored on the remaining data (testing phase). This procedure is repeated k times and yields k training and k testing fold(s), which represent fractions $(k-1)/k$ and $1/k$ of the original dataset, respectively. The reported score is the average of all test set scores. Figure 8 illustrates the procedure. The portion of the dataset that

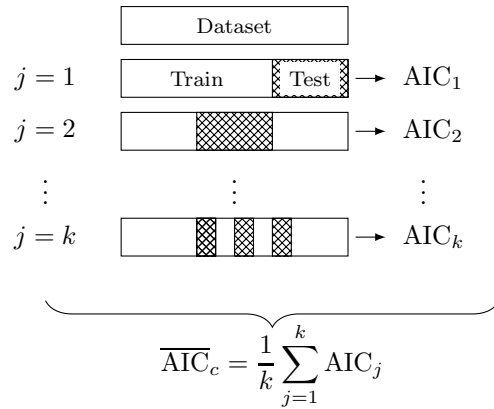


FIG. 8: Schematic of the k -fold method for a given possible combination c of Π -products.

is considered is also randomized (*i.e.*, not contiguous) to avoid bias towards any particular cathode. We use $k = 10$ folds in this study.

The exhaustive grid search yields the following set of Π -products: $(\Pi_2, \Pi_4, \Pi_5, \Pi_7)$. The results are similar to

the first “randomization” iteration: both Π_3 and Π_6 are not necessary to explain most of the variation in the data.

Restricted number of variables We now restrict the maximum number of variables that can be included in the regression and perform the exhaustive grid search again. Table IV shows the Π product combination with the “best” score and the corresponding coefficients, R^2 , and average error, respectively. The results are similar to the second iteration of the randomization process: Π_2 and Π_7 are shown to be the additional Π -products that can be removed from the linear regression if the fit is restricted to two parameters. If the maximum number of variables is restricted to one, the remaining Π -product is Π_5 . The corresponding expression is similar to that obtained with an isentropic flow model and echoes the near-linear relationship between Π_1 and Π_5 : $\Pi_1 \propto \Pi_5$. However, the multiplicative constant obtained with the least-squares fit is different from the theoretical value for isentropic flow. The difference arises from the inclusion of other plasma effects in our model.

IV. DISCUSSION

A. Physical explanation

The four dimensions removed from the original Π -product relationship are Π_2 , Π_3 , Π_6 , and Π_7 . Because most cathodes studied operate with xenon (identical ionization energy), ϵ_{iz} does not show much variation in the dataset. The remaining terms in Π_6 are related to the geometry (orifice diameter, d_o) and the magnetic pressure and are better captured by the other geometric Π -products (Π_2 and Π_3) and Π_5 .

The Reynolds number (Π_7), cathode orifice-to-insert diameter ratio (Π_2), and cathode orifice diameter-to-length ratio (Π_3) are limited to nearly a single order of magnitude: 90% of the calculated Reynolds numbers, Π_2 , and Π_3 lie between 1.3 and 15, 0.07 and 0.5, and 0.2 and 3.7, respectively. More variation in the data is needed to assess where these Π -products are relevant.

Π_4 , which represents the mass utilization or ionization fraction, and ratio of gasdynamic to magnetic pressure (Π_5) can account for most of the variation in the data.

TABLE IV: Π -product combination for multiple maximum number of allowed Π -products.

Number of parameters	Π -product set	β_0	β_1	β_2	β_3	β_4	β_5	β_6	R^2	Average error (%)
1	Π_5	0.64	0	0	0	0.98	0	0	0.94	45.3
≤ 2	Π_4, Π_5	3.95	0	0	-0.28	1.13	0	0	0.96	32.2
≤ 3	Π_2, Π_4, Π_5	5.07	0.44	0	-0.35	1.22	0	0	0.97	30.5
≥ 4	$\Pi_2, \Pi_4, \Pi_5, \Pi_7$	5.80	0.71	0	-0.41	1.22	0	0.33	0.98	23.5

Both the gasdynamic and plasma effects are relevant in this context and represent two mechanisms for pressure changes due to changes in mass flow rate, current, or both.

B. Limitations

The proposed scaling relationship and analysis are limited by the data on which they rely. The analysis does not apply to cathodes which operate with a much longer orifice or a propellant with a much lower ionization energy (*e.g.*, lithium). Although the relationship spans five orders of magnitude in variation of the non-dimensional variables, it would be difficult to confidently extrapolate the relationship outside the bounds of the dataset for some of these parameters because the variation in some Π -products (*e.g.*, the orifice aspect ratio, Π_3) is much smaller than in others. Finally, it is likely that the true dependence of the pressure on the Π -products does not follow a power law. Although the latter is a simplification, it is useful for rapid estimation of the total pressure.

C. Link to theory

Can the simplified Π -product result be derived from theory? Using the scaling law for the total pressure in cathodes we derived from first principles in 59 we now attempt to obtain a semi-empirical relationship for the non-dimensional Π -products.

1. Simple theoretical model

Under the assumption that the momentum flux of heavy particles on the orifice plate and the magnetic pressure are negligible, the scaling law for the total pressure in cathodes we derived in 59 from the plasma momentum balance can be written in its simplest form as:

$$\Pi_1 = C(\alpha_o, T_{e,o}, T_n, \text{Kn}, \gamma) \Pi_5 \quad (42)$$

where C is a scaling factor that includes transitional flow effects and depends non-linearly on the operating conditions through the orifice electron temperature, $T_{e,o}$, ionization fraction, α_o , neutral (static) gas temperature, T_n , and the Knudsen number. In the absence of reliable data for the values on which the scaling factor depends, C can

be found through a fit to the entire experimental dataset with a 95% confidence interval: $C_{\text{exp}} \approx 4.03 \pm 0.22$.

As suggested by the statistical analysis and shown in Figure 9(a), Π_5 is able to account for much of the variation in the data. The R^2 and average error are 0.94 and 46.1%, respectively. While the relationship is similar to the isentropic flow equation (Equation 35), the scaling factor $C(\alpha_o, T_{e,o}, T_n, \text{Kn}, \gamma)$ differs from that obtained with the isentropic flow model. The results of the statistical analysis and Equation 42 indicate that most of the variance in total pressure in hollow cathodes can be accounted for by the gasdynamic pressure modified to incorporate transitional flow effects and changes in the gas constant due to the plasma (see, *e.g.*, 64) through $C(\alpha_o, T_{e,o}, T_n, \text{Kn}, \gamma)$.

2. Complete theoretical model

The total pressure inside an orificed hollow cathode (neglecting viscosity) can be represented as a balance between the momentum flux, gasdynamic pressure, and magnetic pressure:⁵⁹

$$P = \left(\frac{1}{4} - \ln \Pi_2 \right) P_{mag} + C(\alpha_o, T_{e,o}, T_n, \text{Kn}, \gamma) P_{gd} + P_{mf}, \quad (43)$$

where P_{mf} is the momentum flux of heavy particles on the orifice plate. The momentum flux is given by:

$$P_{mf} = \left(\frac{r_c^2}{r_o^2} - 1 \right) en_e^{s,\text{ins}} T_{eV}^{\text{ins}} \left(1 + \frac{n_e^{s,\text{ins}}}{n_n^{\text{ins}}} \right), \quad (44)$$

where $n_e^{s,\text{ins}}$ is the insert sheath-edge electron density, n_n^{ins} is the insert neutral density, and T_{eV}^{ins} is the insert electron temperature in V. Excluding the momentum flux term, Equation 43 can be readily expressed in terms of our Π -products:

$$\Pi_1 = \frac{1}{4} - \ln \Pi_2 + C(\alpha_o, T_{e,o}, T_n, \text{Kn}, \gamma) \Pi_5 + \frac{P_{mf}}{P_{mag}}. \quad (45)$$

Multiple functional forms of the momentum flux term P_{mf}/P_{mag} can be tested and cross-validated across the entire dataset using the k -fold and scoring methodologies described previously. We use a power-law representation for the momentum flux scaled by the magnetic pressure and $(\Pi_2^{-2} - 1)$, to capture any other effects:

$$\Pi_1 = \frac{1}{4} - \ln \Pi_2 + \eta_0 \Pi_5 + \eta_1 (\Pi_2^{-2} - 1) \Pi_2^{\eta_2} \Pi_3^{\eta_3} \Pi_4^{\eta_4} \Pi_5^{\eta_5} \Pi_6^{\eta_6}. \quad (46)$$

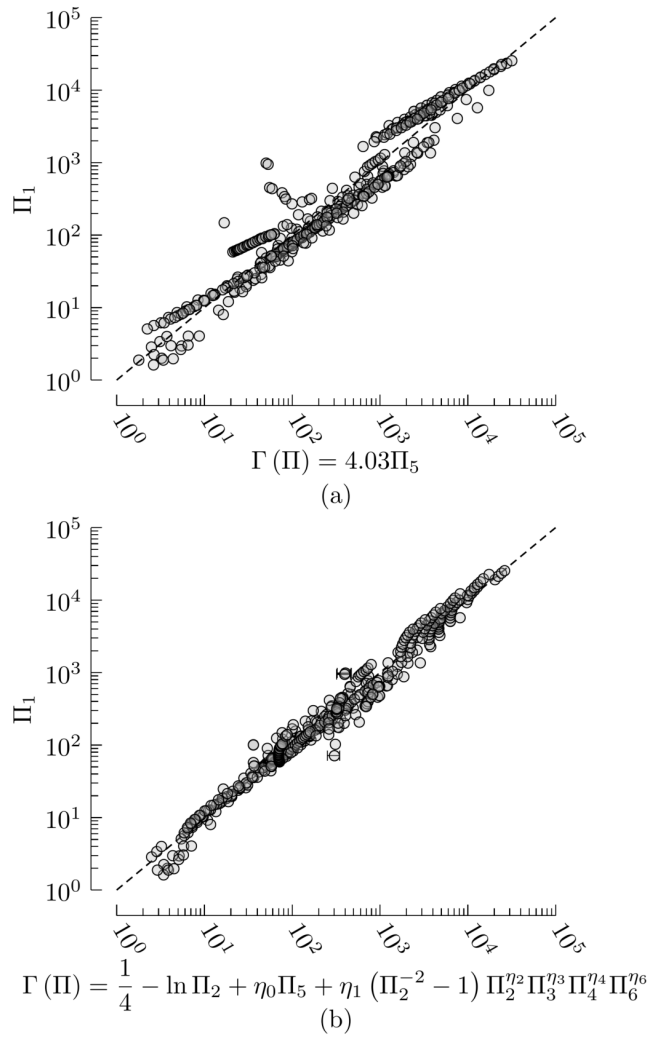


FIG. 9: Theoretically derived expressions applied to the entire experimental dataset. (a) Simplest model (Equation 42) and (b) cross-validated complete model (Equation 52). The horizontal error bars indicate the 95% confidence interval of the predicted Π_1 . Error bars that are smaller than the symbol size are not shown.

Because the original theory does not consider viscosity, we do not include the corresponding Π product (Reynolds number, Π_7) in the power law.

We perform a cross-validated non-linear fit across the entire dataset with the `lmfit` Python package⁶¹ for all possible Π -product combinations that appear in the power law in Equation 46. The total number of combinations is 32 because there are five Π products (Π_2 through Π_6) and because η_1 may be zero.

To help with convergence, we rescale the Π -products that appear in the power law by their respective mean and restrict the search range of the coefficients η_k . Because the momentum flux on the orifice plate and $(\Pi_2^{-2} - 1)$ are positive, η_1 is restricted to positive values. We search for the exponents $\eta_{k,k \geq 2}$ in the (arbitrar-

ily chosen) interval $[-5, 5]$. Finally, we expect η_0 not to vary by more than one order of magnitude. We therefore restrict η_0 to the 1–10 range because the scaling factor C is equal to $C_{\text{theory}} \approx 2.56^{+0.67}_{-0.55}$ for the following range of typical orifice conditions: orifice electron temperature of 2–5 eV, neutral gas temperature of 2000–4000 K, orifice ionization fraction of 1–10%, and Knudsen number of 0.1–10. To obtain this value, we computed the scaling factor C from its theoretical expression:

$$C(\alpha_o, T_{e,o}, T_n, \text{Kn}, \gamma) = \sqrt{1 + \alpha_o T_e^o / T_n} + F(\text{Kn}, \gamma). \quad (47)$$

$F(\text{Kn}, \gamma)$ includes transitional flow effects and is a function of the specific heat ratio and orifice Knudsen number:

$$F(\text{Kn}, \gamma) = \left((1 - \theta) \gamma + \theta \frac{\gamma^{1/2}}{\sqrt{2\pi}} \left(\frac{\gamma + 1}{2} \right)^{1/(\gamma-1)} \right)^{-1}, \quad (48)$$

where θ depends on the Knudsen number. It is given by the empirical expression:⁶⁵

$$\theta = \frac{k_\theta \text{Kn}}{k_\theta \text{Kn} + 1}, \quad (49)$$

where $k_\theta = 28$.

Because we perform a non-linear fit across the entire dataset, an iterative algorithm is required to find the η_k coefficients, which may yield different results depending on the starting point. We also cross-validate the model choice with multiple starting points that are determined by first obtaining η_0 from its theoretical expression (Equation 47), then using this value in a linear regression for the momentum flux scaled by the magnetic pressure and $(\Pi_2^{-2} - 1)$ to determine $\eta_{k,k \geq 1}$:

$$Y_{mf} = \log_{10}(\eta_1) + \sum_{k=2}^6 \eta_k X_{k,mf}, \quad (50)$$

where $X_k = \log_{10} \Pi_k$ and Y_{mf} is given by:

$$Y_{mf} = \log_{10} \left(\frac{\Pi_1 - \left(\frac{1}{4} - \ln \Pi_2 + \eta_0 \Pi_5 \right)}{(\Pi_2^{-2} - 1)} \right). \quad (51)$$

We include up to 20 sets of initial coefficients.

The resulting functional form with the best AIC score is:

$$\Pi_1 = \frac{1}{4} - \ln \Pi_2 + \eta_0 \Pi_5 + \eta_1 (\Pi_2^{-2} - 1) \Pi_2^{\eta_2} \Pi_3^{\eta_3} \Pi_4^{\eta_4} \Pi_6^{\eta_6}. \quad (52)$$

We report the coefficients obtained from the cross-validation procedure in Table V along with their 95% confidence intervals computed with the bootstrap method. The R^2 and average error are 0.98 and 25.4%, respectively. The relationship as applied to the entire normalized pressure dataset is shown in Figure 9(b).

Most of the variation is captured by the aforementioned relationship. Deviations from the theoretical approximation are likely due to plasma and viscous effects that are neglected in Equation 45.

TABLE V: Coefficients for the cross-validated theoretical form and associated 95% confidence interval as computed with the bootstrap method. There are no data for η_5 because the corresponding Π -product is not part of the fit that features the best AIC score.

Coefficient	Lower bound	Value	Upper bound
η_0	2.23	2.44	2.65
η_1	1.84×10^{10}	3.05×10^{12}	1.78×10^{13}
η_2	3.33	3.54	3.80
η_3	-1.67	-1.05	-0.64
η_4	-0.27	-0.20	-0.10
η_5	—	—	—
η_6	0.70	0.79	0.84

V. CONCLUSION

We have performed dimensional and cross-validated statistical analyses of orificed hollow cathode experimental pressure measurements over three orders of magnitude (five orders of magnitude in non-dimensional space) to explain the physical mechanisms that control the total pressure in hollow cathodes. The dimensional analysis indicates that the total pressure (scaled by the magnetic pressure) depends on six non-dimensional parameters, and a principal component analysis suggests that a subset of those parameters can account for the variation in the experimental data. We revealed, through an exhaustive grid search, that the gasdynamic pressure modified to take into account the effect of the plasma (through its effect on the gas constant) can account for most of the variation in the experimental pressure data. We have performed linear and non-linear regression analyses on the experimental data using a variety of pressure models. We have demonstrated that previous empirical and theoretical (Poiseuille and isentropic) flow models cannot account for the variation in the experimental data (unless restricted to a single cathode and a substantial number of pressure measurements are already available), and have shown that an empirical power-law model and the theoretical work from 12 provide qualitative agreement over the entire range of experimental data.

The uncertainty in the neutral gas temperature and viscous and applied magnetic field effects (which were not included in 12) may account for some of the discrepancies observed. We estimated that the pressure drop that occurs between the pressure measurement location and the cathode active zone can be neglected. The pressure measurement is typically performed upstream of the insert plasma and can be multiple cathode lengths away (see, *e.g.*, 28). The relationships derived in this work are

therefore representative of ideal experimental conditions in which the pressure is measured immediately upstream of the insert plasma.

The study demonstrates that previous empirical and theoretical (Poiseuille and isentropic) flow models should not be used to estimate the total pressure inside hollow cathodes, as they cannot account for the variation in the pressure data in most instances. Although the gas flow is laminar and with low insert and orifice Reynolds number ($Re < 100$), *most* of the variation in the data can be accounted for without considering viscous effects. This result does not necessarily imply that the total pressure contribution of viscous effects is negligible. However, because of the lack of *variation* of the Reynolds number in the experimental data, other parameters can more readily account for the variation in the total pressure data (*i.e.*, viscous effects do not change substantially between operating conditions). As shown in our theoretical model,¹² the parameters that can account for the variation in the data include, by order of importance, the gasdynamic pressure modified to take into account the modification of the gas constant due to the plasma and transitional flow effects, the momentum flux of heavy species on the orifice plate, and the magnetic pressure (through the Lorentz force).

DATA AVAILABILITY

The data and software that support the findings of this study are openly available at the following DOI:

- [10.5281/zenodo.3956853](https://doi.org/10.5281/zenodo.3956853): Cathode experimental data and software to assemble the corresponding database.
- [10.5281/zenodo.5765632](https://doi.org/10.5281/zenodo.5765632): Software to reproduce the results presented in this article.

ACKNOWLEDGMENTS

This work was supported by the Princeton Program in Plasma Science and Technology (PPST).

¹A. T. Forrester, D. M. Goebel, and J. T. Crow, *Applied Physics Letters* **33**, 11 (1978).

²S. Tanaka, H. Morita, and J. Sakuraba, *Japanese Journal of Applied Physics* **19**, 1703 (1980).

³P. P. Deichuli, G. F. Abdrashitov, A. A. Ivanov, V. V. Kolmogorov, V. V. Mishagin, G. I. Shul'zhenko, N. V. Stupishin, D. Beals, and R. Granetz, *Review of Scientific Instruments* **77**, 03B514 (2006).

⁴Y. S. Kuo, R. F. Bunshah, and D. Okrent, *Journal of Vacuum Science & Technology A: Vacuum, Surfaces, and Films* **4**, 397 (1986).

⁵A. Lunk, *Vacuum* **41**, 1965 (1990).

⁶H. Morgner, M. Neumann, S. Straach, and M. Krug, *Surface and Coatings Technology* **108–109**, 513 (1998).

⁷J. J. Szabo, B. Pote, R. Tedrake, S. Paintal, L. Byrne, V. J. Hruby, H. Kamhawi, and T. Smith, in *52nd AIAA/SAE/ASEE Joint Propulsion Conference & Exhibit* (2016) AIAA-2016-4830.

This is the author's peer reviewed, accepted manuscript. However, the online version of record will be different from this version once it has been copyedited and typeset.

PLEASE CITE THIS ARTICLE AS DOI: 10.1063/5.0067271

- ⁸J. R. Brophy, Review of Scientific Instruments **73**, 1071 (2002).
- ⁹D. M. Goebel and E. Chu, in *32nd International Electric Propulsion Conference* (2011) IEPC-2011-053.
- ¹⁰R. Hofer, T. Randolph, D. Oh, J. Snyder, and K. de Grys, in *42nd AIAA/ASME/SAE/ASEE Joint Propulsion Conference & Exhibit* (2006) AIAA-2006-4469.
- ¹¹D. L. Brown, B. E. Beal, and J. M. Haas, in *IEEE Aerospace Conference* (2010).
- ¹²P.-Y. C. R. Taunay, C. J. Wordingham, and E. Y. Choueiri, Plasma Sources Science and Technology (2021), submitted.
- ¹³S. J. Hall, B. J. Jorns, A. D. Gallimore, H. Kamhawi, T. W. Haag, J. A. Mackey, J. H. Gilland, P. Y. Peterson, and M. Baird, in *35th International Electric Propulsion Conference* (2017) IEPC-2017-228.
- ¹⁴B. Jorns, A. D. Gallimore, S. J. Hall, P. Y. Peterson, J. E. Gilland, D. M. Goebel, R. Hofer, and I. Mikellides, in *AIAA Propulsion and Energy Forum* (2018) AIAA-2018-4418.
- ¹⁵S. W. Shark, S. J. Hall, B. Jorns, R. R. Hofer, and D. M. Goebel, in *AIAA Propulsion and Energy Forum* (2019) AIAA-2019-3809.
- ¹⁶C. J. Wordingham, P.-Y. C. R. Taunay, and E. Y. Choueiri, Plasma Sources Science and Technology (2021), in press.
- ¹⁷D. E. Siegfried and P. J. Wilbur, in *14th International Electric Propulsion Conference* (1979) AIAA-1979-2056.
- ¹⁸D. E. Siegfried, *A Phenomenological Model for Orificed Hollow Cathodes*, Ph.d., Colorado State University (1982).
- ¹⁹D. E. Siegfried and P. J. Wilbur, AIAA Journal **21**, 5 (1983).
- ²⁰D. E. Siegfried and P. J. Wilbur, AIAA Journal **22**, 1405 (1984).
- ²¹P. J. Wilbur, "Advanced Ion Thruster Research," Tech. Rep. CR-168340 (NASA, 1984).
- ²²D. E. Siegfried and P. J. Wilbur, in *13th International Electric Propulsion Conference* (1978) AIAA-1978-0705.
- ²³A. Salhi and P. J. Turchi, in *23rd International Electric Propulsion Conference* (1993) IEPC-1993-024.
- ²⁴A. Salhi, *Theoretical and experimental studies of orificed, hollow cathode operation*, Ph.d., The Ohio State University (1993).
- ²⁵D. Goebel and I. Katz, *Fundamentals of Electric Propulsion: Ion and Hall Thrusters* (John Wiley & Sons, Inc., 2008).
- ²⁶J. P. Mizrahi, V. Vekselman, Y. Krasik, and V. Gurovich, in *32nd International Electric Propulsion Conference* (2011) IEPC-2011-334.
- ²⁷J. Mizrahi, V. Vekselman, V. Gurovich, and Y. E. Krasik, Journal of Propulsion and Power **28**, 1134 (2012).
- ²⁸M. T. Domonkos, *Evaluation of low-current orificed hollow cathodes*, Ph.d., University of Michigan (1999).
- ²⁹M. T. Domonkos, in *38th AIAA/ASME/SAE/ASEE Joint Propulsion Conference & Exhibit* (2002) AIAA-2002-4240.
- ³⁰R. Albertoni, *Cathode Processes in MPD Thrusters*, Ph. d., Università Degli Studi di Pisa (2012).
- ³¹R. Albertoni, D. Pedrini, F. Paganucci, and M. Andrenucci, IEEE Transactions on Plasma Science **41**, 1731 (2013).
- ³²V. J. Friedly, *Hollow Cathode Operation at High Discharge Currents*, Master's thesis, Colorado State University (1990), M.Sc.
- ³³S. W. Patterson and D. G. Fearn, in *26th International Electric Propulsion Conference* (1999) pp. 695–702, IEPC-1999-125.
- ³⁴P. J. Wilbur, "Ion and Advanced Electric Thruster Research," Tech. Rep. CR-165253 (NASA, 1980).
- ³⁵D. G. Fearn and S. W. Patterson, in *34th AIAA/ASME/SAE/ASEE Joint Propulsion Conference & Exhibit* (1998) AIAA-1998-3346.
- ³⁶D. M. Goebel, K. K. Jameson, and I. Katz, in *40th AIAA/ASME/SAE/ASEE Joint Propulsion Conference & Exhibit* (2004) AIAA-2004-3430.
- ³⁷K. K. Jameson, D. M. Goebel, and R. M. Watkins, in *41st AIAA/ASME/SAE/ASEE Joint Propulsion Conference & Exhibit* (2005) AIAA-2005-3667.
- ³⁸K. K. Jameson, D. M. Goebel, and R. M. Watkins, in *29th International Electric Propulsion Conference* (2005) IEPC-2005-269.
- ³⁹I. G. Mikellides, Physics of Plasmas **16** (2009), 10.1063/1.3056397.
- ⁴⁰J. Polk, A. Grubisic, N. Taheri, D. M. Goebel, and S. E. Hornbeck, in *41st AIAA/ASME/SAE/ASEE Joint Propulsion Conference & Exhibit* (2005) AIAA-2005-4398.
- ⁴¹G. Becatti, D. M. Goebel, J. E. Polk, and P. Guerrero, Journal of Propulsion and Power **34**, 893 (2017).
- ⁴²E. Chu and D. M. Goebel, IEEE Transactions on Plasma Science **40**, 2133 (2012).
- ⁴³This expression can be derived from kinetic theory by assuming a hard-sphere potential for the gas. The mean free path and dynamic viscosity are then given by (see, e.g., 66 pp. 359, 430) $\lambda = m / (\sqrt{2}\pi\sigma^2\rho)$ and $\mu = 5 / (16\pi\sigma^2) \sqrt{\pi m k_B T}$, respectively, where m is the gas atomic mass, ρ the gas mass density, σ the interatomic distance, k_B the Boltzmann constant, and T the gas temperature.
- ⁴⁴L. I. Stiel and G. Thodos, A.I.Ch.E. Journal **7**, 611 (1961).
- ⁴⁵L. F. Epstein and M. D. Powers, The Journal of Physical Chemistry **57**, 336 (1953).
- ⁴⁶N. B. Vargaftik, *Tables on the thermophysical properties of liquids and gases*, 2nd ed. (Hemisphere Publishing Corp., Washington, DC, 1975) p.152.
- ⁴⁷H. v. Tippelskirch, E. U. Franck, F. Hensel, and J. Kestin, Berichte der Bunsengesellschaft für Physikalische Chemie **79**, 889 (1975).
- ⁴⁸A. I. Ivanov, V. E. Lyusternik, and L. R. Fokin, Journal of Engineering Physics **39**, 1360 (1980).
- ⁴⁹V. N. Popov, High Temperature **50**, 700 (2012).
- ⁵⁰P.-Y. C. R. Taunay, *Scaling Laws in Orificed Thermionic Hollow Cathodes*, Ph.d., Princeton University (2020).
- ⁵¹F. White, *Fluid Mechanics, Sixth Edition* (McGraw-Hill Higher Education, 2008) p. 347.
- ⁵²P.-Y. C. R. Taunay, C. J. Wordingham, and E. Y. Choueiri, in *AIAA Propulsion and Energy Forum* (2020) AIAA-2020-3638.
- ⁵³I. G. Mikellides, I. Katz, D. M. Goebel, and J. E. Polk, Journal of Applied Physics **98**, 113303 (2005).
- ⁵⁴L. Cassady, *Lithium-fed Arc Multichannel and Single-Channel Hollow Cathode: Experiment and Theory*, Ph.D. thesis, Princeton University (2006), p.15.
- ⁵⁵G. Sary, L. Garrigues, and J.-P. Boeuf, Plasma Sources Science and Technology **26**, 55007 (2017).
- ⁵⁶E. Buckingham, Physical Review **4**, 345 (1914).
- ⁵⁷E. C. Ipsen, *Units, Dimensions, and Dimensionless Numbers* (McGraw-Hill, 1960).
- ⁵⁸D. M. Goebel, I. Katz, J. E. Polk, I. G. Mikellides, K. K. Jameson, T. Liu, and R. Dougherty, in *Space Conference & Exhibit* (2004) AIAA-2004-5911.
- ⁵⁹P.-Y. C. R. Taunay, C. J. Wordingham, and E. Y. Choueiri, Plasma Sources Science and Technology (2021), submitted.
- ⁶⁰M. Capacci, M. Minucci, and A. Severi, in *33rd AIAA/ASME/SAE/ASEE Joint Propulsion Conference & Exhibit* (1997) AIAA-1997-2791.
- ⁶¹M. Newville, T. Stensitzki, D. B. Allen, and A. Ingargiola, "LM-FIT: Non-Linear Least-Square Minimization and Curve-Fitting for Python," (2014).
- ⁶²F. Pedregosa, G. Varoquaux, A. Gramfort, V. Michel, B. Thirion, O. Grisel, M. Blondel, P. Prettenhofer, R. Weiss, V. Dubourg, J. Vanderplas, A. Passos, D. Cournapeau, M. Brucher, M. Perrot, and E. Duchesnay, Journal of Machine Learning Research **12**, 2825 (2011).
- ⁶³H. Akaike, IEEE Transactions on Automatic Control **19**, 716 (1974).
- ⁶⁴C. H. Chang and E. Pfender, Plasma Chemistry and Plasma Processing **10**, 473 (1990).
- ⁶⁵D. J. Santeler, Journal of Vacuum Science & Technology A: Vacuum, Surfaces, and Films **4**, 348 (1986).
- ⁶⁶D. A. McQuarrie, *Statistical Mechanics* (Harper's Chemistry Series, 1976).